

Photosensitive Field-Effect Transistor with Enhanced Photoamplification Mediated by Charge Transfer in a Heterostructure of α -CsPbI₃ Nanocrystals and Two-Dimensional WS₂

Shreyasi Das¹, Arup Ghorai^{1,2}, Sourabh Pal,³ Somnath Mahato,¹ Soumen Das,⁴ and Samit K. Ray^{1,5,*†}

¹*School of Nano Science and Technology, IIT Kharagpur, Kharagpur, West Bengal, 721302, India*

²*Department of Materials Science and Engineering, Pohang University of Science and Technology, Pohang 790-784, Korea*

³*Advanced Technology Development Centre, IIT Kharagpur, Kharagpur, West Bengal, 721302, India*

⁴*School of Medical Science and Technology, IIT Kharagpur, Kharagpur, West Bengal, 721302, India*

⁵*Department of Physics, IIT Kharagpur, Kharagpur, West Bengal, 721302, India*

(Received 1 November 2022; revised 23 January 2023; accepted 3 February 2023; published 15 March 2023)

Hybrid heterostructure-based phototransistors are attractive owing to their high gain induced by the photogating effect. However, the absence of an in-plane built-in electric field in the single-channel-layer transistor results in a relatively higher dark current and requires a large operating gate voltage of the device. Here, we report air-stable cesium lead iodide/tungsten di-sulfide (CsPbI₃/WS₂) mixed-dimensional heterostructure-based photo-field-effect-transistors (photo-FETs) with asymmetric metal electrodes (Cr/WS₂/Au), exhibiting extremely low dark current (approximately 10⁻¹² A) with a responsivity of approximately 10² A/W at zero gate bias. The Schottky-barrier- (WS₂/Au interface) induced rectification characteristics in the channel accompanied by the excellent photogating effect from solution-processed α -phase CsPbI₃ nanocrystal sensitizers, resulting in gate-tunable broadband photodetection with a very high responsivity (approximately 10⁴ A/W) and excellent sensitivity (approximately 10⁶). Most interestingly, the device shows superior performance even under high-humidity (50–65%) conditions owing to the formation of cubic α -phase CsPbI₃ nanocrystals with a relatively smaller lattice constant ($a = 6.2315 \text{ \AA}$) and filling of surface vacancies (Pb²⁺ centers) with the sulphur atoms from the WS₂ layer, thus protecting it from environmental degradation. These results emphasize an exciting strategy for developing mixed-dimensional hybrid heterostructure-based phototransistors for futuristic integrated nano-optoelectronic systems.

DOI: 10.1103/PhysRevApplied.19.034051

I. INTRODUCTION

Fabrication of high-performance phototransistors demands superior channel material, which should be of high carrier mobility for a high-gain bandwidth product, a direct band gap for efficient optical absorption, a thinner layer for full depletion, leading to ultralow dark current and very low trap state density for low subthreshold swings. Layered semiconducting two-dimensional (2D) transition-metal dichalcogenides (TMDs) fulfil most of these requirements [1–4] making them a potential candidate for a photo-field-effect transistor (photo-FET). However, some trade-offs are found in single-semiconductor-channel-based phototransistors, due to the simultaneous occurrence of both absorption and amplification processes

within the same layer, compromising the device performance [5–7]. To overcome this shortcoming, as well as for fabrication simplicity, attention has been paid to few-layer TMDs over a monolayer with a wider spectral photoresponse and relatively higher absorbance [8–10], which in turn increases the dark-current values requiring a higher gate voltage to operate the device in full depletion mode [11]. This issue can be addressed via incorporating a Schottky barrier by judiciously selecting the metal contacts and utilizing the developed depletion region to facilitate a unidirectional current transport, which leads to the significant lowering of dark current in few layered TMD-based photo-FETs at zero gate bias [12–14]. The built-in electric field of the Schottky interface further helps in the separation of photogenerated charge carriers across the channel layer [15], leading to zero-gate-bias-driven enhanced photosensitivity. WS₂ is one of the useful members of the semiconducting TMD family, having the highest mobility

*physkr@phy.iitkgp.ernet.in

†physkr@phy.iitkgp.ac.in

due to its reduced effective mass and larger valence-band splitting owing to the strong spin-orbit coupling [16,17]. Although mono- and few-layer WS₂ phototransistors have been widely explored, the responsivity of these devices is limited owing to weak optical absorption in thin 2D layers [10,18,19]. For the further improvement of photoresponsivity, recent works are focused on sensitizing the thin channel material with semiconductor nanocrystals (NCs), referred to as sensitizers, having excellent absorption characteristics and opposite doping polarity to create a vertical junction for subsequent charge separation [20–23].

Recently, all-inorganic cesium lead halide (CsPbX₃: X = I, Br, and Cl) perovskite NCs have drawn tremendous interests in the field of optoelectronics [24], featuring superior emissive (approaching photoluminescence quantum yield approximately 100%) [25] characteristics, extremely high absorption coefficient [26], large carrier-diffusion lengths (>3 mm), fast radiative recombination rates, and of note their improved stability [27] over organic-inorganic hybrid perovskites [28,29]. Weerd *et al.* have recently reported colloidal CsPbI₃ NCs with high quantum yield of approximately 98% prepared by hot-injection method, which reveals highly efficient carrier multiplication as well as longer build-up of free-carrier concentration [30]. Particularly colloidal synthesized zero-dimensional (0D) α -CsPbI₃ NCs exhibit an extended photoabsorption band covering the whole visible spectrum with a high absorption coefficient (approximately $3 \times 10^4 \text{ cm}^{-1}$ at 680 nm) [31] and better photo-stability, making them attractive as a photoactive material for high-performance optoelectronic devices under ambient condition. According to the theoretical calculations by Marronnier *et al.*, among four existing phases (α -cubic, β -tetragonal, γ -orthorhombic, and δ -orthorhombic) of CsPbI₃ NCs, α -phase (approximately 1.61 eV) has a lower band gap compared to the β (approximately 1.83 eV) and γ (approximately 2.25 eV) phase perovskites [32]. Further, the rotation of the [PbI₆]⁴⁻ in both γ and β phase leads to destabilizations of the conduction-band minima (CBM). On the other hand, cubic α phase has high stability due to its low surface-to-volume ratio (lattice constant $a = 6.23 \text{ \AA}$) without any octahedral inclination or lattice distortion in the [PbI₆]⁴⁻ octahedra as well as in the unit cell [33–35]. These extraordinary properties of α -phase CsPbI₃ NCs provoke to utilize them as an effective sensitizer in 2D channel-based hybrid phototransistor devices. However, owing to the vulnerability towards moisture for halide perovskite NCs, recently, the surface passivation of CsPbI₃ via coordination of Pb²⁺ centers with sulphur donors has been explored to protect them from environmental degradation [36] to improve the device stability under ambient conditions.

In this work, we present a proof-of-concept for 0D and 2D CsPbI₃/WS₂-based mixed-dimensional van der Waals heterostructure (MvWH) photo-FETs utilizing the

superior photoabsorption attributes of α -phase CsPbI₃ NCs as sensitizers, along with a sub-5-nm-thick 2D WS₂ channel, which acts as an expressway for carrier transport. In our device configuration, the developed built-in electrical field at the CsPbI₃/WS₂ heterostructure facilitates efficient transfer of photogenerated carriers from CsPbI₃ NCs into the WS₂ layer resulting in an excellent broadband visible photoabsorption in the hybrid system. Moreover, asymmetric metal contacts (Au-Cr) as source and drain electrodes are purposefully chosen to utilize the large built-in potential along the WS₂/Au Schottky junction for a diodelike unidirectional current flow and effective separation of photogenerated electron-hole pairs, leading to an excellent rectifying ratio of approximately 10⁴ with a very low dark current of the order of approximately pA under a low source-to-drain bias (V_{DS}) in the absence of a back gate voltage. Fabricated hybrid phototransistor devices exhibit a very high photoresponsivity of approximately 10⁴ A/W at approximately 40 V gate bias upon visible light illumination (approximately 0.1 μW) due to the photogating effect and a broad spectral bandwidth across the entire visible range. In addition, the coordination of sulphur atoms of WS₂ layer with Pb²⁺ centers of CsPbI₃ NCs reveals an excellent device stability under 50–65% humidity condition. Our results are not only exciting in terms of fundamental carrier transport and relaxation pathways in hybrid van der Waals heterojunctions, but also pave the way for constructing high-performance optoelectronic devices using mixed-dimensional 0D and 2D hybrid building blocks, rather than using purely 2D layered materials.

II. EXPERIMENTAL SECTION

A. Synthesis of α -phase CsPbI₃ NCs

This is a two-step reaction, where, in the first-step caesium oleate (Cs-OA) is prepared followed by the synthesis of α -phase CsPbI₃ NCs in the second step.

(i) Firstly, caesium carbonate (Cs₂CO₃) of 814 mg and 40 ml olive oil are added in a round bottom two-neck flask, which is heated at 120 °C for 1 h under vacuum condition. Followed by the rise in temperature to 150 °C under N₂ atmosphere for 10–15 min, the desired transparent solution of Cs-OA is stored for further use to synthesize CsPbI₃.

(ii) Next, 870 mg of PbI₂ and 5 ml of olive oil [instead of 1-octadecene (ODE)] are mixed, which is heated to 120 °C under vacuum for 1 h. Thereafter, we swiftly inject 1 ml of Oleyl amine (OLAm) in the reaction mixture under N₂ atmosphere to get a transparent solution. Finally, preheated (100 °C) Cs-OA is injected to the reaction mixture and cooled immediately in an ice bath to quench the reaction to obtain desired α -phase CsPbI₃ NCs.

Finally, as-synthesized CsPbI_3 is purified through centrifugation using excess hexane. The centrifugation process (20 000 rpm) is repeated for several times to remove excess OLAm/olive oil from the product. Finally, the sedimentation is collected and redispersed in hexane. The collected dispersion is stored in a sealed vial for further characterizations and device fabrications.

B. $\text{CsPbI}_3/\text{WS}_2$ MvWH photo-FET device fabrication

For the fabrication of the $\text{CsPbI}_3/\text{WS}_2$ MvWH photo-FET device, WS_2 flakes are mechanically exfoliated from the bulk WS_2 crystal (2D semiconductor Inc. Scottsdale, AZ, USA) using a Scotch tape (3M Inc. USA) on polydimethylsiloxane (PDMS) gel film (Gel-Pak Inc. Hayward, CA, USA) and the interested few-layer flakes are identified under an optical microscope, followed by the layer confirmation via Raman characteristics and AFM height profile. Note that, mechanically exfoliated flakes are chosen for their high quality and clean interface promising greater mobility and high-performance device fabrication. Further, for the Au contact with WS_2 , electrodes are patterned in advance on a prepatterned SiO_2/Si (285-nm oxide thickness) substrate using e-beam lithography technique and then Cr (5 nm)/Au (30 nm) are deposited via e-beam evaporation followed by lift off with acetone. Then, the selected few-layer flakes are deterministically transferred on the targeted Au electrodes from PDMS gel film following the dry-transfer technique to make sure residue-free clean transfer. After the successful transfer of the flakes on Au electrodes, again electrodes are patterned using second-step e-beam lithography followed by metal deposition Cr (5 nm)/Au (30 nm) for Cr contacts on WS_2 . To remove the resist residue and improve the contact conductance, the fabricated devices are annealed at 150 °C for 2 h in a high vacuum of approximately 10^{-3} Torr. Finally, the 10 μl of synthesized diluted solution (0.1 mg ml^{-1}) of perovskite NCs is uniformly spin-coated several times (varying from one to four) onto the WS_2 layer with a speed of 2000 rpm.

C. Characterizations and measurements

X-ray diffraction (XRD, Philips MRD X-ray diffractometer) patterns are recorded using characteristic $\text{CuK}\alpha$ ($\lambda = 1.5418 \text{ \AA}$) radiation with 2.0° grazing incidence angle. For the TEM sample preparation, CsPbI_3 NCs solution is dissolved in hexane and then placed into a TEM grid and dried for a few minutes and the measurement performed. The TEM images are carried out using TECNAI G2 TF20-ST and JEM-2100F Field Emission Electron Microscope operating at 200 kV equipped with Gaytan's latest CMOS camera. All the images are proceeding by Digital Micrograph Software for the estimation of d spacing and indexing. UV-vis-NIR absorption spectra of as-synthesized CsPbI_3 samples are recorded using a fiber probe-based UV-vis-NIR spectrophotometer (Model:

U-2910 Spectrophotometer, HITACHI) and a broadband light source. Raman and PL spectra are recorded using a semiconductor laser of excitation wavelength 532 nm, equipped with a CCD detector, an optical microscope of $100\times$ objective lens and a spectrometer (WITec alpha-300R). The photogenerated carrier lifetime is measured by exciting the material with a pulsed diode laser of wavelength 372 nm and detecting the signal using Edinburgh LifeSpec-II fluorescence lifetime spectrometer fitted with a PMT detector. Room-temperature current-voltage characteristics are recorded using a Keithly semiconductor parameter analyzer (4200 SCS) in the presence of an argon laser (514 nm) and a broadband solar simulator (AM 1.5, 100 mW/cm²) as a visible light source.

III. RESULTS AND DISCUSSIONS

To study the crystal structure of as-synthesized CsPbI_3 NCs, we record x-ray diffraction pattern, followed by their fitting with Rietveld refinement full proof software, which are presented in Fig. 1(a). An excellent agreement with fitted results indicates the growth of dominantly single-phase (α -phase) cubic CsPbI_3 . The crystal structure of CsPbI_3 NCs visualized using VESTA 3D software through Rietveld fitting is shown in Fig. 1(b). The VESTA 3D (1 × 1) structure shows the absence of any octahedral inclination in the perovskite NCs, which is known to be beneficial for achieving higher stability under laboratory ambient (45–50% humidity). Typical HRTEM image reveals almost cubic shape of the synthesized NCs ($15.05 \times 18.04 \text{ nm}^2$), as shown in Fig. 1(c). Corresponding fast-Fourier-transform (FFT) pattern presented in Fig. 1(d) of the red squared portion of Fig. 1(c), shows pure cubic α -phase pattern along the zone axis [002]. Whereas, the high-resolution fringe pattern from the yellow squared region of Fig. 1(c) shows a d spacing of 0.62 nm, which is well matched with the cubic α phase of CsPbI_3 [35], as shown in Fig. 1(e). The result indicates (100) directional growth of cubic phase CsPbI_3 NCs, which is in good agreement with our previously reported results [35]. Corresponding selected area electron diffraction (SAED) patterns shown in Fig. 1(f), with indexed (200), (220), and (020) planes along the zone axis [004], also corroborate the pure cubic structure of synthesized CsPbI_3 .

Figure 2(a) presents the optical absorption and emission properties of the as-synthesized α -phase CsPbI_3 NCs in the visible wavelength range with an absorption edge extended up to approximately 680 nm and the corresponding direct band-gap value is approximately 1.814 eV [35], as extracted from the Tauc plot shown in Fig. S1 within the Supplemental Material [37]. Further, the PL maxima at approximately 687 nm confirms the formation of excitons (X_α) across the direct band gap (approximately 1.80 eV) of α -phase CsPbI_3 NCs represented via the blue curve in Fig. 2(a). The Gaussian line shape of the PL spectrum and

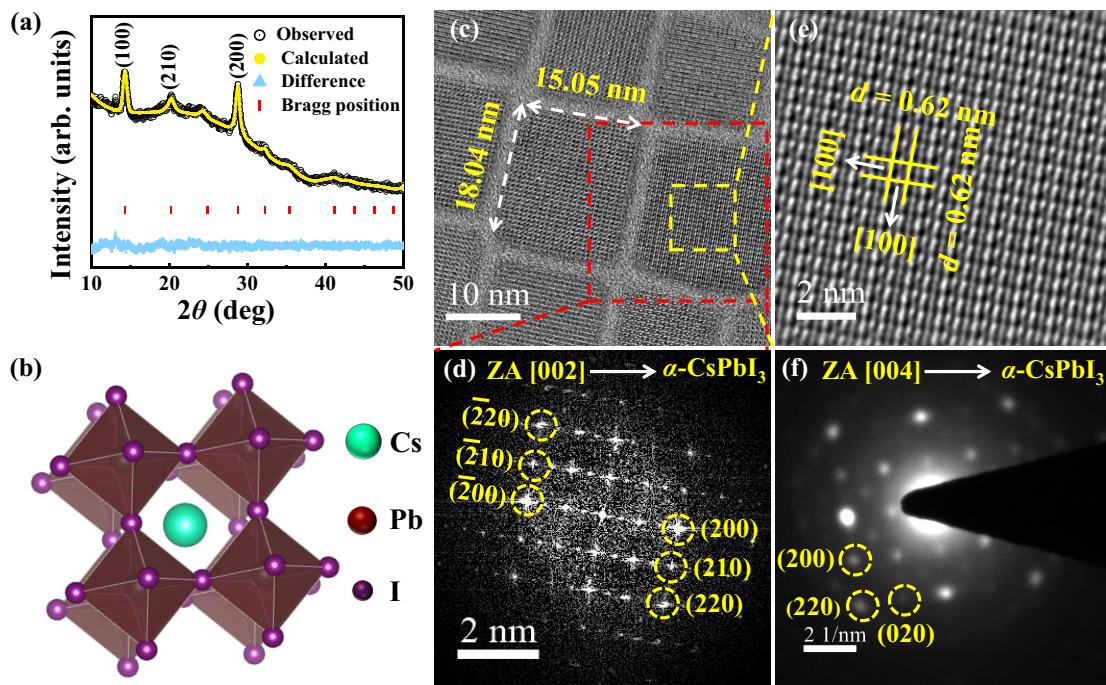


FIG. 1. (a) Rietveld refinements (α -phase fitting) of the XRD pattern of a film of cubic CsPbI_3 NCs. (b) 1×1 3D VESTA visualization image of $\alpha\text{-CsPbI}_3$ cubic crystal structure. (c) Typical HRTEM image of CsPbI_3 NCs with an energy 200 keV revealing cubic morphology. (d) FFT patterns from a region marked by the red dotted square on the micrograph (c). (e) A magnified view of the corresponding HRTEM image in the selected yellow square region on micrograph (c). (f) SAED pattern of $\alpha\text{-CsPbI}_3$ NCs showing well-defined diffraction spots indexed as (200), (220), and (020) planes viewed along the [004] zone axis.

the absence of any other PL peaks clearly supports the synthesis of pure α -phase CsPbI_3 without the presence of any mixed phase. Further, the extracted direct band-gap nature from the Tauc plot and strong photoluminescence attributes of as-synthesized $\alpha\text{-CsPbI}_3$ nanocrystals make them a potential candidate as a light sensitizer material. To examine the charge-transfer mechanism at the CsPbI_3 NCs/WS₂ interface, Raman spectroscopy and micro-PL ($\mu\text{-PL}$) measurements are carried out by spin coating of a dilute solution of CsPbI_3 NCs uniformly on the exfoliated WS₂ surface. For the room-temperature $\mu\text{-Raman-PL}$ measurements, samples have been excited with a cw laser having a wavelength of 532 nm with the laser power being kept at a very low value to avoid any local-heating-induced sample degradation. Figure 2(b) represents comparative Raman spectra of WS₂ and mixed-dimensional van der Waals heterostructure (MvWH) samples, showing intense in-plane 2LA + E_{2g}^1 Raman modes at approximately 351 cm⁻¹ and out-of-plane vibrational A_{1g} peaks at approximately 420 cm⁻¹ [38]. The A_{1g} vibrational Raman mode, which preserves the symmetry of the lattice, is clearly red shifted by approximately 4.7 cm⁻¹ in the case of the CsPbI_3 -decorated WS₂ layer [inset of Fig. 2(b)], revealing the interfacial charge-transfer phenomena. The external electron doping in 2D WS₂ leads to the filling up of antibonding states of the conduction band, mostly

made up of d_z^2 orbitals of transition-metal atoms [39]. This makes the bonds weaker and the A_{1g} peak of pristine WS₂ is shifted towards a lower wave number on significant electron doping from CsPbI_3 NCs [40].

On the other hand, the monolayer (ML) WS₂ PL-emission characteristics [Fig. 2(c)(i)] consist of a strong A^- excitonic emission at approximately 1.995 eV, corresponding to the direct band-to-band transitions at the K (and/or K') point of the Brillouin zone, and a weaker trionic A^- emission at approximately 1.965 eV with a binding energy of approximately 30 meV, which are in good agreement with the previously reported results [40]. Further, the sublinear variation in the double logarithmic plot of deconvoluted PL-peak-integrated intensity with laser power (Fig. S2 within the Supplemental Material [37]) confirms the emissions attributing to neutral excitons (A) and trions (A⁻) from ML WS₂ [40,41]. It is to be noted that, ML WS₂ is purposefully chosen for the charge-transfer study via PL measurements due to its extraordinary luminescence property at room temperature owing to the direct band-gap transition. The existence of trions in the room-temperature emission spectrum indicates the unintentional doping in the unpassivated WS₂ flake from the substrate as well as the surrounding environment [42,43]. A systematic PL study of the hybrid structure with increasing layer numbers of CsPbI_3 NCs spin coated

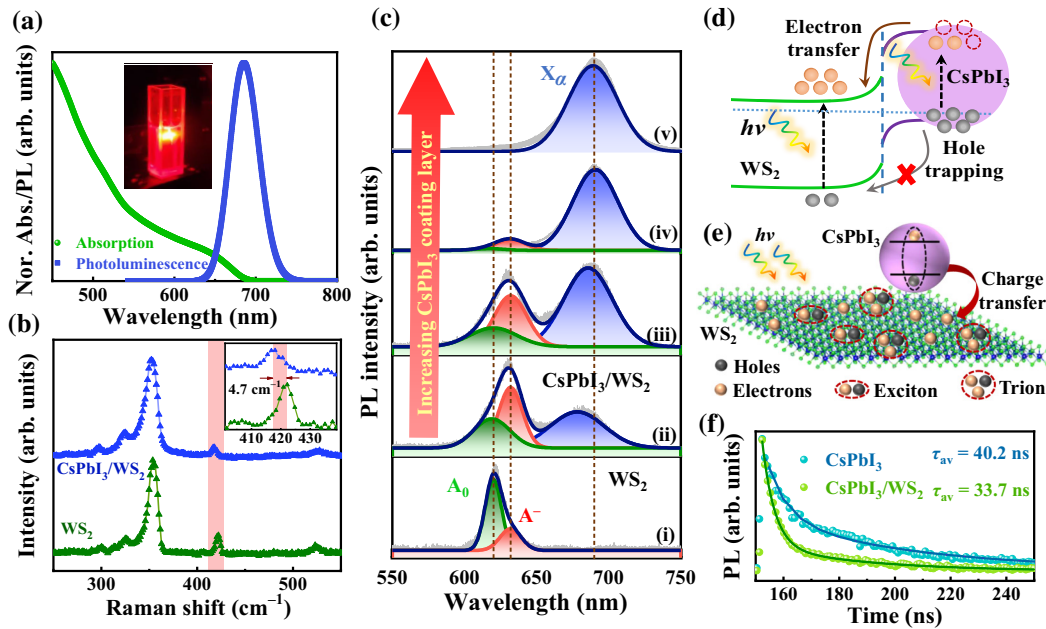


FIG. 2. (a) Absorption (green) and photoluminescence (blue) spectra of as-synthesized cubic phase CsPbI_3 NCs. (b) Comparative Raman spectra of WS_2 flakes before and after CsPbI_3 NCs' decoration showing characteristic E_{2g} and A_{1g} peaks of layered WS_2 . Inset shows the magnified image of the out-of-plane A_{1g} mode revealing a clear peak shift to lower wave numbers due to electron doping in WS_2 flakes from CsPbI_3 NCs. (c) Deconvoluted PL spectra of (i) a bare ML WS_2 flake and (ii-v) the heterostructure samples with varying number of spin-coated layers of CsPbI_3 NCs on the WS_2 flake. The spectra (ii), (iii), (iv), and (v) represent the PL emission from the first, second, third, and fourth spin-coated layers of CsPbI_3 NCs, respectively. The green (red) peak represents the A^- excitonic (trion) emission from ML WS_2 flakes and the blue peak represents the emission from band-to-band transition of cubic α -phase CsPbI_3 NCs. (d) Energy-band diagram of $\text{CsPbI}_3/\text{WS}_2$ hybrid heterostructures showing effective electron doping in WS_2 from CsPbI_3 sensitizers and hole trapping in the NCs giving rise to a strong photogating effect. (e) Schematic representation of the charge-transfer mechanism in 0D and 2D $\text{CsPbI}_3/\text{WS}_2$ hybrid heterostructures giving rise to trion formation in ML WS_2 . (f) Normalized time-resolved PL decay curves of CsPbI_3 NCs (blue curve) and $\text{CsPbI}_3/\text{WS}_2$ hybrids (red curve), measured using an excitation wavelength of 372 nm.

over ML WS_2 shows a pronounced excitonic-PL quenching in MvWH as compared to both the pristine materials (Fig. S3 within the Supplemental Material [37]). Further, the $\text{CsPbI}_3/\text{WS}_2$ MvWHs show relatively broad PL spectra with combined contributions from CsPbI_3 NCs as well as ML WS_2 and the spectral shape changes with increasing CsPbI_3 spin-coated layer numbers [Fig. 2(c)(ii-v)]. To explore the effect of CsPbI_3 coating over WS_2 , we fit each spectrum with three Gaussian peaks containing the characteristics of the excitonic features of both the materials and analyzed their intensity variation with increasing concentration of CsPbI_3 treated on WS_2 flakes, as shown in Fig. 2(c). It is noticed that the distinctive trion peak (A^-) of WS_2 becomes prominent with increasing density (coating number) of CsPbI_3 NCs and finally excitonic-to-trionic (integrated intensity) crossover is observed above a critical concentration of CsPbI_3 NCs (Fig. S4 within the Supplemental Material [37]). The possible explanation behind these observations is as follows: upon illumination, photoexcited electron-hole pairs are generated in both WS_2 and CsPbI_3 , however, due to the type-II energy-band alignment of the heterostructures, electrons are easily transferred from CsPbI_3 NCs to ML WS_2 , as illustrated in

Fig. 2(d). On the other hand, photogenerated holes remain trapped in the NCs, resulting in a reduced recombination rate and giving rise to a quenched excitonic PL intensity for CsPbI_3 NCs and increased trionic emission in ML WS_2 . The enhanced generation rate of trions results in the reduced density of excitons inside the system, leading to the suppression of excitonic peak intensity and the dominance of the trion peak in the PL spectra of MvWH, as schematically depicted in Fig. 2(e) [40]. To further confirm the charge-transfer phenomena, time-resolved photoluminescence (TR-PL) spectra are measured. Figure 2(f) shows the TR-PL decay curves of CsPbI_3 NCs (blue curve) and $\text{CsPbI}_3/\text{WS}_2$ MvWHs (red curve). The PL decay curves are fitted using a biexponential function to extract the average excitonic life time (τ_{av}). The τ_{av} of CsPbI_3 NCs decreases from 40.2 to 33.7 ns after hybridization with WS_2 , corroborating the successful charge-transfer mechanism from CsPbI_3 NCs to WS_2 flakes [44–46]. As a conclusion, the type-II band alignment in $\text{CsPbI}_3/\text{WS}_2$ heterostructure facilitates an efficient electron-hole pair separation and strong electron doping into the WS_2 channel, making the hybrid system ideal for fabrication of superior performance phototransistor devices [47].

The CsPbI_3 NCs/ WS_2 MvWH photo-FET with asymmetric metal contacts is demonstrated by exploiting the Schottky-barrier-induced dark-current suppression for the zero-gate-bias-driven photosensitivity of the device with a simpler fabrication technique. Figure 3(a) schematically demonstrates the as-fabricated phototransistor device structure consisting of a few-layer WS_2 channel and asymmetric Cr and Au electrodes as source and drain terminals, respectively. The inset shows the optical micrograph of the connected few-layer WS_2 flake ($5 \times 2 \mu\text{m}^2$) having a thickness of approximately 4.5 nm corresponding to four–five atomic layers of WS_2 , further corroborated by the AFM analysis (Fig. S5 within the Supplemental Material [37]). The deposition of a lower work function Cr ($\Phi_{\text{Cr}}=4.5 \text{ eV}$) and higher work function Au ($\Phi_{\text{Au}}=5.1 \text{ eV}$) on *n*-type WS_2 as asymmetric contacts reveals room-temperature rectifying diode characteristics with rectification ratio up to 5.2×10^2 even at zero applied back gate bias, as depicted via the current-voltage (I_{DS} - V_{DS}) characteristics in Fig. 3(b). Under an applied reverse drain voltage, the potential barrier height between Au and WS_2 becomes higher to suppress the current flow through the junction compared to Cr, and thus exhibits the I_{DS} - V_{DS} characteristics of an ideal diode [13]. The I - V characteristics is fitted with the Richardson-Schottky Eq. (A1) as depicted in Fig. S6 within the Supplemental Material [37] with the extracted barrier potential (Φ_B) value approximately 0.588 eV, an ideality factor (η) approximately 2.09 and a series resistance of approximately $800 \text{ M}\Omega$. The origin of a relatively higher ideality factor is the presence of interfacial defects at the metal-semiconductor interface. The proposed asymmetric metallization scheme breaks the mirror symmetry of the built-in potential profile within the channel, which facilitates the reduction of the dark current significantly, making the device architecture an ideal prototype for operating in full depletion mode even at zero gate bias, leading to a very high sensitivity of the device [48,49]. On the other hand, a linear I_{DS} - V_{DS} characteristics with a comparatively larger current value (100 nA) confirms the formation of an Ohmic-like junction with a very low contact resistance ($250 \text{ M}\Omega$) for Cr- WS_2 -Cr device [50]. Further, the Au- WS_2 -Au system reveals a rectifying output characteristics with relatively lower current than Cr contacts, confirming a typical high resistive back-to-back Schottky diode [15]. We fit the curve considering the presence of two Schottky barriers at both contacts and the estimated Schottky-barrier height is 0.553 and 0.523 eV, indicating the presence of two equal Schottky barriers in the Au- WS_2 -Au device [48] (Fig. S6 within the Supplemental Material [37]). The energy-band alignment with different metal contacts is schematically depicted in Fig. S7 within the Supplemental Material [37], revealing an easy current flow through the Ohmic Cr junction and restricted flow via built-in potential barrier in the Au Schottky junction. Figure 3(c) shows the transfer (I_{DS} - V_{GS})

characteristics of the WS_2 phototransistor with asymmetric Cr-Au contacts under dark condition at a reverse drain voltage of -2 V , revealing excellent *n*-type channel properties at room temperature with *off* currents of the order of 10 pA and a transistor *on*:*off* ratio approximately 10^4 . Further, to understand the effect of CsPbI_3 treatment on the device performance, the CsPbI_3 / WS_2 hybrid transistor characteristics is compared with the pristine WS_2 one, referred to as the control device. The incorporation of sensitizing perovskite NCs on the 2D- WS_2 layer results in a junction formation via Fermi-level alignment in equilibrium under dark condition. In this case, there will be an adequate electron flow from WS_2 to CsPbI_3 side, as electrons in WS_2 have a higher energy than those in CsPbI_3 . The draining of electrons from the WS_2 channel to CsPbI_3 NCs leads to the depletion of majority carriers in the WS_2 channel resulting in the lowering of the current flow under dark condition. Further, we study the output characteristics of the hybrid phototransistor under dark condition on application of gate voltage varying from 10 to 40 V, as depicted in Fig. 3(d). For a higher positive gate voltage, more electrons are induced in the WS_2 channel and the transistor has a higher current in the saturation state. On the other hand, under a negative gate bias a small amount of current flows through the channel owing to the depletion of carriers, leading to the *off* state of the transistor [Fig. 3(c)].

The performance of the CsPbI_3 / WS_2 MvWH photo-FET is analyzed by recording the room-temperature I_{DS} - V_{DS} characteristics for zero gate bias under dark as well as visible illumination using a Newport solar simulator having broadband emission with irradiance of 100 mW/cm^2 under air mass (AM) 1.5G condition, as shown in Fig. 4(a). For comparison, the characteristics of the pristine WS_2 control device is also presented. The suppression of dark current to the order of tens of pA even without any gate bias along with the significant reduction of noise currents are attributed to the built-in electric field at the Au- WS_2 Schottky junction, which further helps in effective separation of photogenerated carriers created in the WS_2 channel.

On illuminating the heterojunction device, the reverse current tends to increase due to the collection of photogenerated minority carriers (holes) at the electrodes. The photo-to-dark current ratio of MvWH photo-FETs by illuminating with a broadband light source is estimated to be much higher compared to the pristine WS_2 one (approximately 1000 times) under the applied reverse-bias condition, which reaches a value of approximately 1.08×10^6 at V_{DS} of -2 V , as shown in Fig. S8 within the Supplemental Material [37]. The decoration of the WS_2 channel with superior light-absorbing perovskite CsPbI_3 NCs facilitates enhancement in the photocurrent by elevating the photogenerated carriers in the channel via efficient charge transfer from CsPbI_3 to WS_2 due to type-II

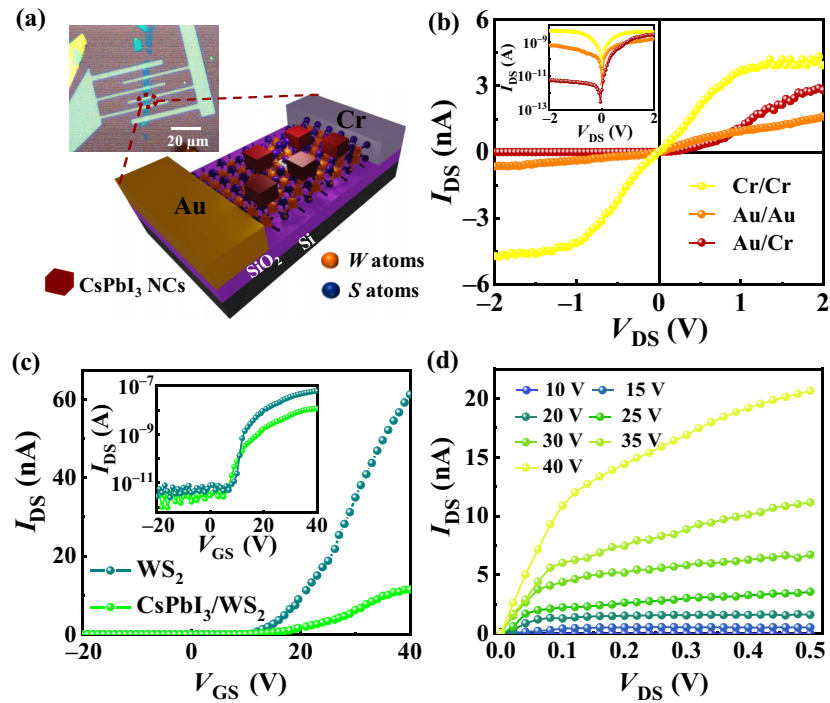


FIG. 3. (a) Schematic 3D view of the fabricated back-gated phototransistor comprising of CsPbI₃ sensitized WS₂ channel with asymmetric electrodes (Au and Cr) acting as a source and drain. An optical micrograph of the device is shown in the inset. (b) Linear I_{DS} - V_{DS} characteristics of three fabricated devices with different source-drain contacts (i) Cr-Cr (yellow curve), (ii) Au-Au (orange curve), and (iii) Au-Cr (brown curve) without any back gate bias. Inset: the corresponding semilogarithmic I_{DS} - V_{DS} characteristics plots. (c) Transfer (I_{DS} - V_{GS}) characteristics of the CsPbI₃/WS₂ hybrid transistor (green curve) and control WS₂ transistor (blue curve) devices in linear scale and logarithmic scale (inset). The current value in the accumulation region decreases and the threshold voltage is shifted to a higher positive voltage in the hybrid device due to charge transfer through the CsPbI₃/WS₂ junction. (d) Output characteristics of the hybrid device with varying gate voltage.

energy-band alignment [7,23]. This explains the significant enhancement (approximately 10³ times) of response of MvWH transistor over the control one, revealing the role of photoabsorbing CsPbI₃ NCs in boosting the performance of the phototransistor. Further, the spectral responsivity of the fabricated MvWH photo-FET, the most useful figure of merit to evaluate a detector performance, is studied displaying a broadband spectral photoresponse covering the entire visible wavelength range, as shown in Fig. 4(b). It may be noted that a peak responsivity of approximately 1.05×10^2 A/W at approximately 460 nm at an applied bias (V_{DS}) of -2 V is achieved, which is close to the C-exciton absorption edge of WS₂. Two other peaks at approximately 620 nm ($R \sim 0.97 \times 10^2$ A/W) and approximately 720 nm ($R \sim 0.77 \times 10^2$ A/W) correspond to the direct band-gap absorption of few layer WS₂ and α -phase CsPbI₃ NCs, respectively. Further, the spectral responsivity increases with increasing reverse V_{DS} that assists in the efficient extraction of photogenerated carriers. On the other hand, the control WS₂-based device also exhibits a similar trend with increasing bias showing a maximum peak responsivity of approximately 10 A/W at approximately

460 nm at -2 V applied V_{DS} (Fig. S9 within the Supplemental Material [37]). It is to be noted that the decoration of CsPbI₃ NCs on WS₂ flakes not only improves the detector responsivity by more than ten-fold but also extends the spectral responsivity window up to 800 nm, as shown comparatively in Fig. 4(b). Hence, the decoration of the WS₂ active channel layer with excellent photoabsorbing CsPbI₃ NCs appear to be a promising approach for next-generation high-performance optoelectronic applications. To further investigate the role of CsPbI₃ in photocarrier generation and efficient charge transfer, the electromagnetic simulations are performed using the COMSOL Multiphysics software. Figure 4(c) shows the electric field distribution of the hybrid CsPbI₃/WS₂ device, illuminated with an electromagnetic plane wave of wavelength $\lambda = 680$ nm from the top, which propagates through air and the nanostructure. The distribution clearly depicts that the electric field is trapped along the edges of the nanocubes of CsPbI₃ with the maximum confinement occurring near the base (as demonstrated by the color index profile), resulting in strong charge transport in the CsPbI₃/WS₂ hybrid heterostructure.

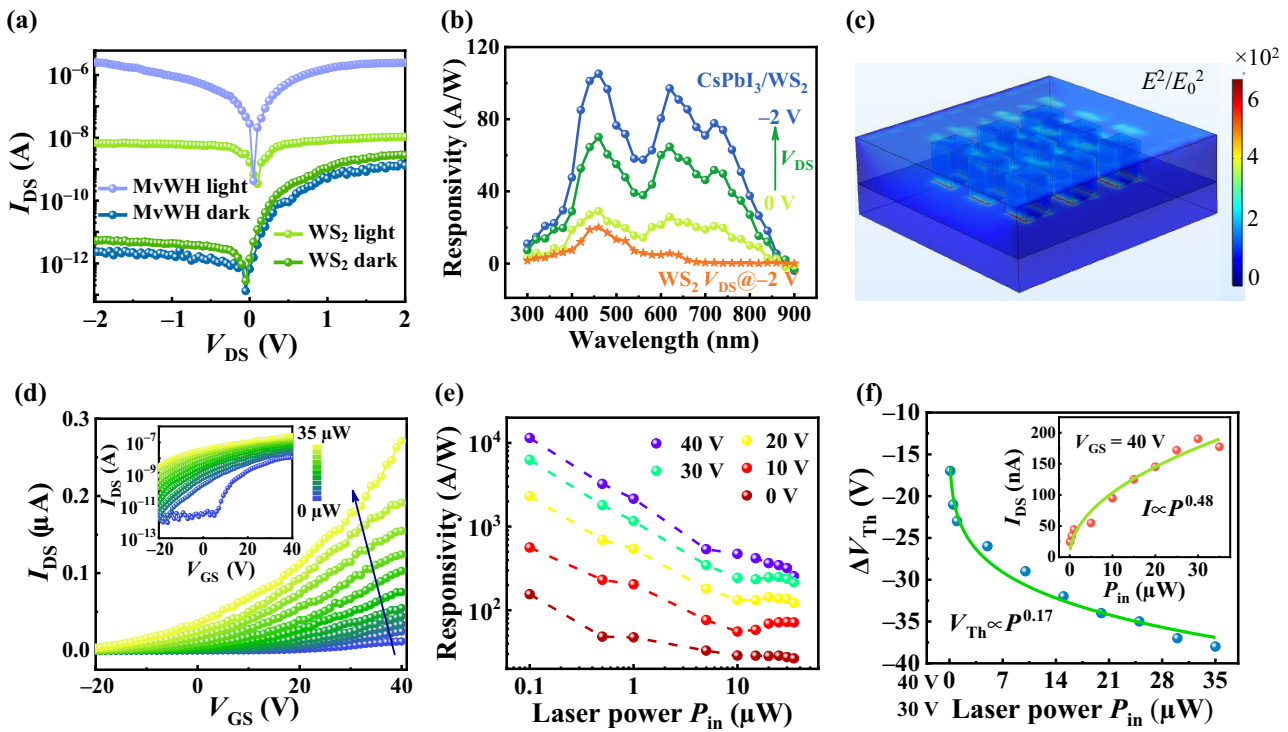


FIG. 4. (a) Comparative I_{DS} - V_{DS} characteristics of pristine WS_2 and $CsPbI_3/WS_2$ MvWH photo-FET under dark and illumination via broadband light source for zero gate bias. (b) Spectral responsivity curves of MvWH photo-FET at $V_{GS} = 0$ V with increasing reverse V_{DS} from 0 to -2 V, as shown via yellow, green, and blue curves. The blue curve represents the responsivity of the photo-FET at a maximum V_{DS} of -2 V, while the spectral responsivity of the control device (orange curve) showing an order of magnitude lower device response at the same V_{DS} . (c) COMSOL Multiphysics simulated E -field distribution at the vicinity of the hybrid system upon excitation with an excitation wavelength of 680 nm. (d) The transfer characteristics (I_{DS} - V_{GS}) of MvWH photo-FET for a range of incident powers (from 0.1 to 35 μ W) with an illumination of wavelength 514 nm at $V_{DS} = -2$ V. (e) The variation of responsivity of the device with incident illumination power for V_{GS} varying from 0 to 40 V. (f) The shift in threshold voltage (ΔV_{th}) with increasing illumination power (P_{in}) fitted with a power law. Blue dots represent the extracted data points from (a) and the green line represents the fitted curve. Inset: the power-law fit of the variation of photocurrent with incident power at $V_{DS} = -2$ V and $V_{GS} = 40$ V showing a sublinear photocurrent dependency with incident optical power.

Further to explore the impact of gate bias on transistor performance, the photoinduced transfer characteristics (I_{DS} - V_{GS}) of the $WS_2/CsPbI_3$ MvWH photo-FET is recorded under the dark (black markers) and 514 -nm illumination with a range of optical powers (from 0.1 to 35 μ W) at a constant V_{DS} of -2 V, as illustrated in Fig. 4(d). The corresponding logarithmic current representation is depicted in the inset. Under illumination of a fixed power of 35 μ W, the drain current of the MvWH photo-FET is enhanced by approximately 13 times (from approximately 20 nA to approximately 0.26 μ A) at a constant gate voltage of approximately 40 V, manifested by the strong photoabsorption in $CsPbI_3$ and subsequent transfer of photoexcited electrons to the WS_2 channel. Further, with the increase of laser power, the photocurrent significantly increases in the accumulation region (i.e., $V_{GS} > V_{th}$) and the transfer curves are gradually shifted to a negative gate voltage. As illustrated in Fig. 2(d), the favorable energy-band alignment rules out the possibility of hole injection

from $CsPbI_3$ into WS_2 , leading to the trapped-hole-induced strong photogating effect in the hybrid system [51]. This leads to significant photocurrent increment in the accumulation region and negative threshold voltage shift (ΔV_{th}) with increasing incident power density of illumination [45]. To investigate in greater detail, the calculated responsivity as a function of illumination power is plotted for different gate-bias voltages in Fig. 4(e). Here, the responsivity value increases with increasing positive gate bias in case of MvWH photo-FETs and reaches to a high value of approximately 1.1×10^4 A W $^{-1}$ at a back gate voltage of approximately 40 V under an illumination power of 0.1 μ W. Further, for all the gate voltages, the measured responsivity dropped with increasing power because of the saturation of sensitizing traps in $CsPbI_3$ NCs, which is a characteristic footprint of trap-dominated photoreponse [52–54]. Despite using higher values of illumination power, the extracted responsivity of our device is quite remarkable, as compared to those previously reported 0D

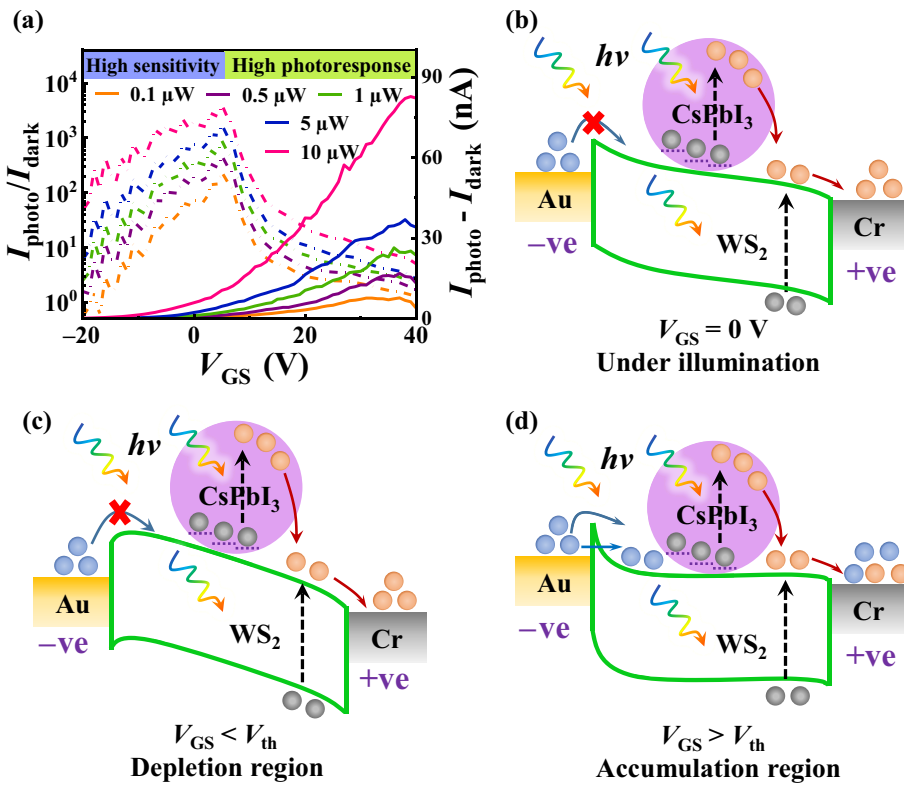


FIG. 5. (a) Back-gate bias-dependent photocurrent (right axis) and photo-to-dark current ratio, (left axis) of the phototransistor device under five different illumination intensities (from 0.1 to 10 μW) for 514 nm. Despite the strongest photoresponse at higher gate bias ($V_{\text{GS}} \approx 40$ V), the highest sensitivity of the device is achieved in the depletion regime ($V_{\text{GS}} \approx 0$ V). The schematic representation of channel current transport mechanism and energy band diagram of the asymmetric contact hybrid phototransistor under reverse drain-source voltage with (b) zero and (c) and (d) different gate-bias conditions.

and 2D hybrid phototransistors [45,47] for similar power levels. The specific detectivity (D^*), which is another useful figure of merit of a photodetector, is estimated using the following equation [55]:

$$D^* = \frac{\sqrt{AB}}{\text{NEP}} = \frac{R\sqrt{A}}{S_n}, \quad (1)$$

where, NEP is the noise equivalent power, R is the responsivity, A is the optically active area of the detector, B is the noise bandwidth, and S_n is the noise spectral density of the device. The frequency-dependent noise spectral density of the device is presented as Fig. S10 within the Supplemental Material [37]. The calculated specific detectivity value for the hybrid device is estimated to be approximately 1.26×10^{13} Jones at $V_{DS} = 1$ V and $V_{GS} = 40$ V. We extract the threshold voltage via extrapolating the linear region of each transfer curve under different incident laser powers and the shift in threshold voltage is plotted as a function of incident power. The variation is fitted with the power-law function $V_{\text{th}} \propto P^b$, as depicted in Fig. 4(f), to understand the possible photoconduction mechanism. The extracted fitting exponent, $b \sim 0.17$ clearly indicates

a sublinear dependency on laser power confirming the existence of photogating-dominant carrier conduction in MvWH photo-FETs [56]. Further, it is also observed that the change in V_{th} is large in the lower power region and starts to saturate gradually at a higher power owing to the saturated trap states present in sensitizer interface leading to the saturation of the photogating effect. The photocurrent $I_{\text{ph}} = I_{\text{photo}} - I_{\text{dark}}$ versus gate voltage for different illumination intensity [Fig. 5(a)] shows a strong modulation with V_{GS} , and a clear maximum in response can be identified around +35 V. The strongest response of the FET device corresponds to the region with highest transconductance, due to the favorable Fermi-level alignment, for low-contact resistance operation leading to many cycles of electron circulation to produce maximum gain. Hitherto, in this region the FET device operates at a relatively higher dark current, compromising the SNR of the device, which is also a very useful figure of merit of photo-FETs.

The SNR defined as $I_{\text{photo}}/I_{\text{dark}}$ is illustrated in the same panel in Fig. 5(a), which reveals the potential of 0D and 2D hybrid phototransistors for the highest sensitivity detection in its depletion regime with V_{GS} from 0 to 5 V. In this region, a lower dark current and a maximum

TABLE I. Comparison of device performances with reported 2D-material-based hybrid photo-FETs with perovskite sensitizers.

Device structure	Sensitizer	Operational spectral range	$I_{\text{dark w/o applied } V_{GS}}$	$I_{\text{photo}}/I_{\text{dark}} @ V_{GS} = 0 \text{ V}$	Responsivity @ different V_{GS}	Detectivity (Jones)	Ref.
Au/MLWS ₂ /Au	CH ₃ NH ₃ PbI ₃ films	450–700 nm	5 nA	10 ⁴	2.5 A/W @ 0 V	10 ¹²	[57]
Au/MLMoS ₂ /Au	CsPbBr ₃ nanosheets	350–550 nm	0.2 nA	10 ³	4.4 A/W @ 0 V	—	[58]
Au/Ti/MLMoS ₂ /Ti/Au	CH ₃ NH ₃ PbBr ₃ / CsPbI _{3-x} Br _x quantum dots	532 and 355 nm	4 nA	10 ⁴	$7 \times 10^4 \text{ A/W @ 60 V}$	1.9×10^{12}	[59]
Au/Ti/FLMoS ₂ /Ti/Au	CsPbBr ₃ quantum dots	405 nm	10 nA	10	$4.7 \times 10^4 \text{ A/W @ 20 V}$	—	[60]
Au/FL BP/Au	CsPbBr ₃ nanocrystals	405 nm	2 nA	10 ²	357.2 mA/W @ 0 V	2.6×10^{11}	[61]
Au/MLMoS ₂ /Au	CsPbI _{3-x} Br _x quantum dots	532 nm	0.2 μA	10 ³	$1.13 \times 10^5 \text{ A/W @ 60 V}$	—	[62]
Au/FL BP/Al/Au	MAPbI _{3-x} Cl _x layer	400–900 nm	0.1 μA/μm	10 ²	$4 \times 10^6 \text{ A/W @ 40 V}$	9×10^{13}	[63]
Au/Ti/FLMoSe ₂ (WSe ₂)/Ti/Au	CsPb(Cl/Br) ₃ quantum dots	455 nm	0.8 nA	10	10^2 A/W @ 50 V	—	[64]
Au/Cr/FLTa ₂ NiSe ₅ /Cr/Au	CH ₃ NH ₃ PbI ₃ quantum dots	800 nm	3.5 μA	10	$2.4 \times 10^2 \text{ A/W @ 0 V}$	6×10^{12}	[47]
Au/Cr/FL WS ₂ /Au/Cr	α-phase CsPbI ₃ nanocrystals	400–800 nm	2 pA	10 ⁶	10^4 A/W @ 40 V	1.2×10^{13}	Our work

sensitivity are achieved, despite the device's concurrent drop in the photocurrent. So the maximum sensitivity of the device can be achieved via contact engineering where the transistor is operated in the depletion region, even without applying any gate bias, hitherto unreported for photo-FET devices. While the peak responsivity of our device is comparable or superior to the reported 2D-material-based hybrid phototransistor devices with perovskite sensitizers, the sensitivity is found to be significantly higher without application of any external gate bias (see Table I). These results illustrate the superior performance of broadband phototransistor, with ultrahigh sensitivity and responsivity, using the CsPbI₃ NCs' sensitized 2D WS₂ layer.

On the other hand, a remarkable photoresponse of CsPbI₃/WS₂ MvWH photo-FET is explained by considering the influence of positive gate voltage on energy-band alignment at the contact interfaces and heterostructures leading to efficient charge injection into *n*-type WS₂ channel layer from photoabsorbing CsPbI₃ NCs. As illustrated in Fig. 5(b), the Schottky barrier at the Au/WS₂ interface is high enough to inhibit the charge conduction mechanism across the WS₂ channel layer at reverse drain bias without any gate electric field under dark condition. Hence, the transistor immediately goes to the *off* state with very low dark current in the order of pA. At this condition, when the visible light is illuminated on the 0D and 2D heterostructure, the photogeneration takes place in both CsPbI₃ NCs as well as the WS₂ channel layer, as depicted in Fig. 5(b). The effective photogenerated carrier separation takes place by the built-in electric field at the Schottky junction (WS₂/Au) as well as at CsPbI₃/WS₂ interfaces. The subsequent transition of photoexcited electrons from CsPbI₃ to WS₂ starts to populate the active channel layer, which are collected by the external electrodes under an applied reverse V_{DS} , leading to the photoresponsivity of approximately 10^2 A/W at $V_{DS} = -2 \text{ V}$ and $V_{GS} = 0 \text{ V}$. Further, the application of a back gate voltage (V_{GS}) to the device modulates the Schottky barrier height at Au/WS₂ interface as shown in Figs. 5(c) and 5(d) [65,66]. An application of negative gate bias ($V_{GS} < V_{th}$) increases the barrier height leading to the transistor operation in the depletion region, where the photosensitivity ($I_{\text{photo}}/I_{\text{dark}}$) of the device is maximum. On the other hand, on increasing the V_{GS} beyond V_{th} initiates the lowering of the Schottky barrier at the Au/WS₂ interface, resulting in a higher magnitude of charge-carrier injection from the Au electrode to the WS₂ channel layer through thermoionic as well as tunneling mechanisms, as illustrated in Fig. 5(d). Thus, the cumulative effects of CsPbI₃ NCs' decoration-mediated strong photogating phenomena as well as the gate-voltage-induced Schottky barrier lowering result in a drastic enhancement of the photocurrent ($I_{\text{photo}} - I_{\text{dark}}$) through the transistor channel at *on* state ($V_{GS} > V_{th}$). This leads to an ultrahigh photoresponsivity of the order of approximately 10^4 A/W

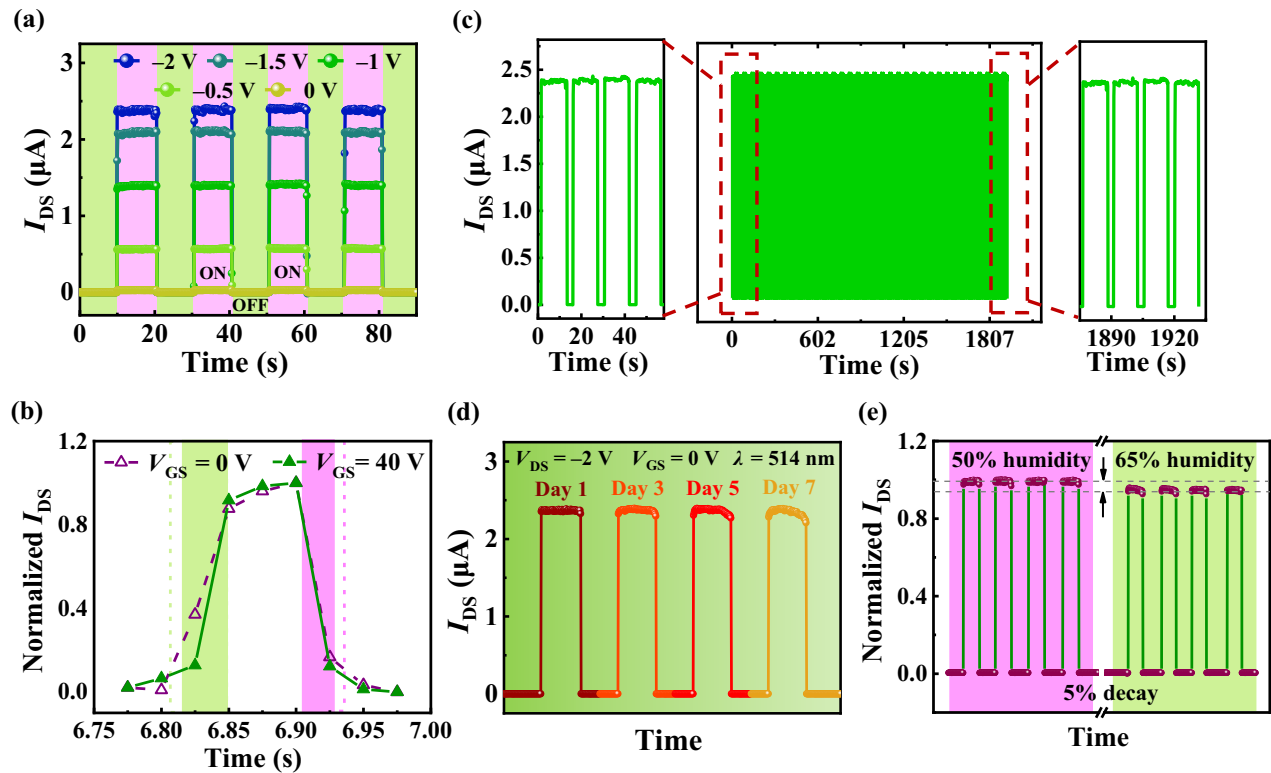


FIG. 6. (a) Transient response of the MvWH photo-FET device under illumination of a 514-nm laser at different applied V_{DS} . (b) Temporal photocurrent response of the MvWH device for a wavelength of 514 nm with and without any applied gate bias. The temporal response indicates a significant decrease in rise time (from 43.8 to 34 ms) as well as fall time (from 32.7 to 24 ms), measured at a relatively higher power of 35 μW . (c) Operational stability of the fabricated MvWH photo-FET device under visible illumination for more than half an hour. (d) The transient photocurrent response of the fabricated transistor over a span of 7 days from the beginning and end of the stability test. (e) Stability of the device tested under extreme humid conditions (varying from 50 to 65% RH). The last four cycle is the response under 65% of humidity showing around 5% decay in the photoresponse.

at $V_{GS} = 40 \text{ V}$. Such gate-modulated responsivity and sensitivity of MvWH photo-FET devices via interface engineering is fascinating for next-generation high-performance and low-power-integrated photonic technology.

Temporal photoresponse is also a useful parameter for the phototransistors' performance in terms of switching speed and device stability. The transient photoresponse of the as-fabricated $\text{CsPbI}_3/\text{WS}_2$ MvWH photo-FET upon visible illumination ($\lambda = 514 \text{ nm}$) at $V_{GS} = 0 \text{ V}$ with varying reverse V_{DS} is demonstrated in Fig. 6(a). Upon illumination of four periodic pulses of the argon-ion laser, relatively fast and consistent photocurrent modulation characteristics of the device reveals the stability and reproducibility of the as-fabricated MvWH photo-FET. The device exhibits a much stronger photoresponse characteristics revealing *on:off* ratio of approximately 10^6 as compared to the control device with pristine WS_2 with the value approximately 10^3 (Fig. S11 within the Supplemental Material [37]), which is attributed to the injection of high-density photogenerated charge carriers into the WS_2 channel from strong light-absorbing CsPbI_3 NCs. With the increment of reverse V_{DS} , a consistent photocurrent

enhancement is distinctly noticed from the switching characteristics owing to the increase of depletion-region width at the Schottky barrier interface and subsequent separation of photogenerated charge carriers. Further, the rise and fall times of the fabricated device in the absence of gate bias are estimated using an enlarged single-cycle response [Fig. 6(b)] and are found to be around approximately 43.8 and approximately 32.7 ms, respectively, which are further reduced to 34 and 24 ms, respectively on applying a gate voltage of 40 V. The response speed of these devices are found to be relatively slower, which is attributed to the trapping of charge carriers in various structural and surface-defect states present in WS_2 as well as CsPbI_3 NCs and their local junction interfaces. These interface traps present in the WS_2 layer are mostly empty when biased under depletion condition, i.e., $V_{GS} < V_{th}$ owing to lack of enough mobile carriers in the channel. This allows a large number of photogenerated electrons to get trapped by the defect states while some of the gate-induced electrons, although small in number, can be trapped as well. This results in a relatively slow rise of current, as depicted in the photocurrent dynamic response. On the other hand,

the interface traps are nearly filled up with gate-induced electrons in accumulation condition, when $V_{GS} > V_{th}$, as shown in Fig. 6(b). Hence, the trapping probability of photogenerated carriers is lower and a relatively faster response (approximately 34 ms) is observed in MvWH photo-FET devices. Further, owing to the fact that the perovskite materials are prone to environmental degradation via oxygen diffusion through iodide vacancies upon illumination, the long-term operation stability of the fabricated devices are tested in this study upon visible light illumination at zero gate bias for prolonged duration (more than 60 min). From the $I-t$ curves for the first 100 s [Fig. 6(c), left] and the last 100 s [Fig. 6(c), right], it is observed that the photocurrent has almost no attenuation, indicating that these devices show an excellent light stability under ambient condition, even without the use of a glovebox or encapsulation. The device stability has also been tested via recording the photocurrent under illumination over a period of one week, as illustrated in Fig. 6(d). Here, the phototransistor sustains under laboratory ambient conditions [relative humidity (RH) approximately 45–50%, temperature approximately 22 °C] for one week with negligible change in the photocurrent via degradation after storing. Further, as CsPbI₃ NCs are vulnerable to environmental humidity, to explore the device performance in the extreme humid condition, we perform the temporal response under 65% RH showing an insignificant degradation (5% decay) in terms of device response [Fig. 6(e)]. This superior performance stability is due to the surface-defect passivation of CsPbI₃ through the interaction with the sulphur of WS₂ ensuring the outstanding environmental stability of as-fabricated CsPbI₃/WS₂ MvWH photo-FETs. The sulphur atoms present on the top layer of WS₂ may have stronger coordination to the Pb²⁺ centers of CsPbI₃ NCs leads to reduced defect states in perovskites enabling higher reluctance to the degradation [36]. It may be noted that the performance of the devices could be further improved by process optimization, device encapsulation, and incorporation of buffer layers. This work reveals the significant potential of colloidal synthesized air-stable α-CsPbI₃ NCs on 2D materials in fabricating 0D and 2D mixed-dimensional heterostructure photo-FETs for applications in next-generation optoelectronic devices.

IV. CONCLUSION

To summarize, significant improvements in performance are realized in CsPbI₃/WS₂ 0D and 2D mixed-dimensional phototransistors with asymmetric metal electrodes leading to combinatorial effect of Schottky-barrier-induced suppression of dark current and efficient charge transfer from photoabsorbing CsPbI₃ nanocrystals, resulting in enhanced photosensitivity and spectral responsivity. The WS₂ channel with asymmetric contacts

(Cr/WS₂/Au) shows a rectifying $I-V$ characteristics under an applied V_{DS} with the dark current in the order of pA. Further, by combining the channel sensitization via decorating the WS₂ with photosensitive air-stable α-phase CsPbI₃ NCs, a responsivity of approximately 10² A/W is achieved at low V_{DS} (approximately –2 V) for an incident optical power of 0.1 μW even without any external gate bias. The device exhibits a broad spectral photoresponsivity between 400 and 800 nm due to the extended visible-light absorption features of CsPbI₃ NCs. Using gate-controlled carrier modulation in the transistor channel, a peak responsivity approximately 10⁴ A/W ($V_{GS} = 40$ V) is achieved owing to the photogating-effect-mediated charge conduction whereas the maximum sensitivity (approximately 10⁶ at approximately $V_{DS} = -2$ V) in terms of signal-to-noise ratio is observed by depleting the channel carries ($V_{GS} = 0$ to 5 V). These devices show superior performance in terms of environment stability, owing to the filling of surface trap states present in CsPbI₃ NCs via conjugation with sulphur atoms of the 2D WS₂ layer. The fabricated hybrid heterostructure devices combining 2D TMDs and superior light absorbing 0D perovskite nanocrystals, through proper interface engineering, would open up pathways for advanced optoelectronic functionalities and energy-harvesting applications.

ACKNOWLEDGMENTS

S.K.R. acknowledges the support of Chair Professor Fellowship of the Indian National Academy of Engineering (INAE).

CONFLICTS OF INTEREST

There are no conflicts to declare.

APPENDIX: THE MODELING OF DARK $I_{DS}-V_{DS}$ CHARACTERISTICS OF WS₂ TRANSISTOR

The dark $I_{DS}-V_{DS}$ characteristics of all three types of metal-semiconductor contact pairs (Au/Cr, Cr/Cr, and Au/Au) are modeled with appropriate current-voltage relations and represented as Figs. S6(a)–S6(c) within the Supplemental Material [37]. Figure S6(a) within the Supplemental Material [37] represents a typical diode like asymmetric $I_{DS}-V_{DS}$ characteristics of the WS₂ phototransistor with one Cr and the other Au contacts with a high rectification factor of approximately 10³ under 2 V applied V_{DS} (2.8 nA @ 2 V; 5.3 pA @ –2 V). We model the curve with the Richardson-Schottky equation [Eqs. (A1) and (A2)] and the extracted barrier potential (Φ_B) is approximately 0.588 eV and the ideality factor (η) is approximately 2.09.

$$I_T = I_S [e^{(qV/\eta kT)} - 1], \quad (A1)$$

$$I_S = SA^* T^2 e^{-(\Phi_B/kT)}. \quad (A2)$$

Figure S6(b) within the Supplemental Material [37] represents linear I_{DS} - V_{DS} characteristics of WS₂ phototransistor with symmetric Cr/Cr contacts. From the literature the WS₂ electron affinity ranges from 3.74 to 4.6 eV, while the Cr work function is 4.5 eV. Hence, Cr electrodes with a low work function ($\Phi_{Cr}=4.5$ eV) form an Ohmic-like junction with WS₂, which we model with the linear current equation [Eq. (A3)], and the extracted conductance value is 3.99×10^{-9} A/V from the fitting.

$$I_T = V/R. \quad (\text{A3})$$

Finally, Fig. S6(c) within the Supplemental Material [37] reveals almost symmetric nonlinear I_{DS} - V_{DS} characteristics of WS₂ phototransistor with both side Au contacts. As, *n*-type WS₂ is in contact with a higher work-function metal ($\Phi_{Au}=5.1$ eV), back-to-back Schottky junctions with relatively high resistive contacts are formed. So, we model the I_{DS} - V_{DS} characteristics considering the double Schottky barrier [Eq. (A4)] and the barrier heights are found to be 0.553 and 0.523 eV, respectively, for two different Au contacts, which are almost similar [48].

$$I_T = \frac{2I_{S1}I_{S2} \sinh(qV/2kT)}{[I_{S1}e^{(qV/2kT)} + I_{S2}e^{(qV/2kT)}]}, \quad (\text{A4})$$

$$I_{S1,2} = S_1 A^* T^2 e^{-(\Phi_{B1,2}/kT)}. \quad (\text{A5})$$

- [1] K. S. Novoselov, D. Jiang, F. Schedin, T. J. Booth, V. V. Khotkevich, S. V. Morozov, and A. K. Geim, Two-dimensional atomic crystals, *Proc. Natl. Acad. Sci. U. S. A.* **102**, 10451 (2005).
- [2] J. Pu, Y. Yomogida, K.-K. Liu, L.-J. Li, Y. Iwasa, and T. Takenobu, Highly flexible MoS₂ thin-film transistors with ion gel dielectrics, *Nano Lett.* **12**, 4013 (2012).
- [3] B. Radisavljevic, A. Radenovic, J. Brivio, V. Giacometti, and A. Kis, Single-layer MoS₂ transistors, *Nat. Nanotechnol.* **6**, 147 (2011).
- [4] K. F. Mak, C. Lee, J. Hone, J. Shan, and T. F. Heinz, Atomically Thin MoS₂: A New Direct-Gap Semiconductor, *Phys. Rev. Lett.* **105**, 136805 (2010).
- [5] D. Kufer and G. Konstantatos, Photo-FETs: Phototransistors enabled by 2D and 0D nanomaterials, *ACS Photonics* **3**, 2197 (2016).
- [6] N. Huo, S. Gupta, and G. Konstantatos, MoS₂-HgTe quantum dot hybrid photodetectors beyond 2 μm, *Adv. Mater.* **29**, 1606576 (2017).
- [7] G. Konstantatos, M. Badioli, L. Gaudreau, J. Osmond, M. Bernechea, F. P. G. de Arquer, F. Gatti, and F. H. L. Koppens, Hybrid graphene–quantum dot phototransistors with ultrahigh gain, *Nat. Nanotechnol.* **7**, 363 (2012).
- [8] W. Choi, M. Y. Cho, A. Konar, J. H. Lee, G.-B. Cha, S. C. Hong, S. Kim, J. Kim, D. Jena, J. Joo, and S. Kim, High-detectivity multilayer MoS₂ phototransistors with spectral response from ultraviolet to infrared, *Adv. Mater.* **24**, 5832 (2012).

- [9] J. Kwon, Y. K. Hong, G. Han, I. Omkaram, W. Choi, S. Kim, and Y. Yoon, Giant photoamplification in indirect-bandgap multilayer MoS₂ phototransistors with local bottom-gate structures, *Adv. Mater.* **27**, 2224 (2015).
- [10] N. Perea-López, A. L. Elías, A. Berkdemir, A. Castro-Beltran, H. R. Gutiérrez, S. Feng, R. Lv, T. Hayashi, F. López-Urías, S. Ghosh, *et al.*, Photosensor device based on few-layered WS₂ films, *Adv. Funct. Mater.* **23**, 5511 (2013).
- [11] K. Natori, Ballistic metal-oxide-semiconductor field effect transistor, *J. Appl. Phys.* **76**, 4879 (1994).
- [12] D. Li, X. Sun, H. Song, Z. Li, H. Jiang, Y. Chen, G. Miao, and B. Shen, Effect of asymmetric Schottky barrier on GaN-based metal-semiconductor-metal ultraviolet detector, *Appl. Phys. Lett.* **99**, 261102 (2011).
- [13] J. Kim, A. Venkatesan, N. A. N. Phan, Y. Kim, H. Kim, D. Whang, and G. Kim, Schottky diode with asymmetric metal contacts on WS₂, *Adv. Electron. Mater.* **8**, 2100941 (2022).
- [14] M. Fontana, T. Deppe, A. K. Boyd, M. Rinzan, A. Y. Liu, M. Paranjape, and P. Barbara, Electron-hole transport and photovoltaic effect in gated MoS₂ Schottky junctions, *Sci. Rep.* **3**, 1634 (2013).
- [15] J.-Y. Wu, Y. T. Chun, S. Li, T. Zhang, and D. Chu, Electrical rectifying and photosensing property of schottky diode based on MoS₂, *ACS Appl. Mater. Interfaces* **10**, 24613 (2018).
- [16] H. R. Gutiérrez, N. Perea-López, A. L. Elías, A. Berkdemir, B. Wang, R. Lv, F. López-Urías, V. H. Crespi, H. Terrones, and M. Terrones, Extraordinary room-temperature photoluminescence in triangular WS₂ monolayers, *Nano Lett.* **13**, 3447 (2013).
- [17] H.-P. Komsa and A. V. Krasheninnikov, Electronic structures and optical properties of realistic transition metal dichalcogenide heterostructures from first principles, *Phys. Rev. B* **88**, 085318 (2013).
- [18] N. Huo, S. Yang, Z. Wei, S.-S. Li, J.-B. Xia, and J. Li, Photoresponsive and gas sensing field-effect transistors based on multilayer WS₂ nanoflakes, *Sci. Rep.* **4**, 5209 (2014).
- [19] S. Hwan Lee, D. Lee, W. Sik Hwang, E. Hwang, D. Jena, and W. Jong Yoo, High-performance photocurrent generation from two-dimensional WS₂ field-effect transistors, *Appl. Phys. Lett.* **104**, 193113 (2014).
- [20] S. Zhang, X. Wang, Y. Chen, G. Wu, Y. Tang, L. Zhu, H. Wang, W. Jiang, L. Sun, T. Lin, *et al.*, Ultrasensitive hybrid MoS₂–ZnCdSe quantum dot photodetectors with high gain, *ACS Appl. Mater. Interfaces* **11**, 23667 (2019).
- [21] D.-H. Kwak, P. Ramasamy, Y.-S. Lee, M.-H. Jeong, and J.-S. Lee, High-performance hybrid InP QDs/black phosphorus photodetector, *ACS Appl. Mater. Interfaces* **11**, 29041 (2019).
- [22] Y. Lee, J. Kwon, E. Hwang, C.-H. Ra, W. J. Yoo, J.-H. Ahn, J. H. Park, and J. H. Cho, High-performance perovskite-graphene hybrid photodetector, *Adv. Mater.* **27**, 41 (2015).
- [23] Z. Sun, Z. Liu, J. Li, G. Tai, S.-P. Lau, and F. Yan, Infrared photodetectors based on CVD-grown graphene and PbS quantum dots with ultrahigh responsivity, *Adv. Mater.* **24**, 5878 (2012).
- [24] S. Pal, A. Ghorai, D. K. Goswami, and S. K. Ray, Strain mediated light emission using heterojunctions of all-inorganic mixed-halide perovskite nanocrystals via piezophototronic effect, *Nano Energy* **87**, 106200 (2021).

- [25] F. Liu, Y. Zhang, C. Ding, S. Kobayashi, T. Izuishi, N. Nakazawa, T. Toyoda, T. Ohta, S. Hayase, T. Minemoto, *et al.*, Highly luminescent phase-stable CsPbI_3 perovskite quantum dots achieving near 100% absolute photoluminescence quantum yield, *ACS Nano* **11**, 10373 (2017).
- [26] A. Ghorai, S. Mahato, S. K. Srivastava, and S. K. Ray, Atomic insights of stable, monodispersed $\text{CsPbI}_{3-x}\text{Br}_x$ ($x = 0, 1, 2, 3$) nanocrystals synthesized by modified ligand cell, *Adv. Funct. Mater.* **32**, 2202087 (2022).
- [27] A. Ghorai, A. Midya, and S. K. Ray, Surfactant-induced anion exchange and morphological evolution for composition-controlled caesium lead halide perovskites with tunable optical properties, *ACS Omega* **4**, 12948 (2019).
- [28] M. A. Becker, R. Vaxenburg, G. Nedelcu, P. C. Sercel, A. Shabaev, M. J. Mehl, J. G. Michopoulos, S. G. Lambrakos, N. Bernstein, J. L. Lyons, *et al.*, Bright triplet excitons in caesium lead halide perovskites, *Nature* **553**, 189 (2018).
- [29] Q. A. Akkerman, G. Rainò, M. V. Kovalenko, and L. Manna, Genesis, challenges and opportunities for colloidal lead halide perovskite nanocrystals, *Nat. Mater.* **17**, 394 (2018).
- [30] C. de Weerd, L. Gomez, A. Capretti, D. M. Lebrun, E. Matsubara, J. Lin, M. Ashida, F. C. M. Spoor, L. D. A. Siebbeles, A. J. Houtepen, *et al.*, Efficient carrier multiplication in CsPbI_3 perovskite nanocrystals, *Nat. Commun.* **9**, 4199 (2018).
- [31] K. M. Sim, A. Swarnkar, A. Nag, and D. S. Chung, Phase stabilized $\alpha\text{-CsPbI}_3$ perovskite nanocrystals for photodiode applications, *Laser Photonics Rev.* **12**, 1 (2018).
- [32] A. Marronnier, G. Roma, S. Boyer-Richard, L. Pedesseau, J. M. Jancu, Y. Bonnassieux, C. Katan, C. C. Stoumpos, M. G. Kanatzidis, and J. Even, Anharmonicity and disorder in the black phases of cesium lead iodide used for stable inorganic perovskite solar cells, *ACS Nano* **12**, 3477 (2018).
- [33] T. Wu, Y. Wang, Z. Dai, D. Cui, T. Wang, X. Meng, E. Bi, X. Yang, and L. Han, Efficient and stable CsPbI_3 solar cells via regulating lattice distortion with surface organic terminal groups, *Adv. Mater.* **31**, 1900605 (2019).
- [34] J.-K. Sun, S. Huang, X.-Z. Liu, Q. Xu, Q.-H. Zhang, W.-J. Jiang, D.-J. Xue, J.-C. Xu, J.-Y. Ma, J. Ding, *et al.*, Polar solvent induced lattice distortion of cubic CsPbI_3 nanocubes and hierarchical self-assembly into orthorhombic single-crystalline nanowires, *J. Am. Chem. Soc.* **140**, 11705 (2018).
- [35] S. Mahato, A. Ghorai, A. Mondal, S. K. Srivastava, M. Modak, S. Das, and S. K. Ray, Atomic-scale imaging and nano-scale mapping of cubic $\alpha\text{-CsPbI}_3$ perovskite nanocrystals for inverted perovskite solar cells, *ACS Appl. Mater. Interfaces* **14**, 9711 (2022).
- [36] J. C. Hamill, O. Romiluyi, S. A. Thomas, J. Cetola, J. Schwartz, M. F. Toney, P. Clancy, and Y.-L. Loo, Sulfur-donor solvents strongly coordinate Pb^{2+} in hybrid organic-inorganic perovskite precursor solutions, *J. Phys. Chem. C* **124**, 14496 (2020).
- [37] See Supplemental Material at <http://link.aps.org/supplemental/10.1103/PhysRevApplied.19.034051> for detailed material and device characterizations.
- [38] A. Berkdemir, H. R. Gutiérrez, A. R. Botello-Méndez, N. Perea-López, A. L. Elías, C.-I. Chia, B. Wang, V. H. Crespi, F. López-Urías, J. Charlier, *et al.*, Identification of individual and few layers of WS_2 using Raman spectroscopy, *Sci. Rep.* **3**, 1755 (2013).
- [39] B. Chakraborty, A. Bera, D. V. S. Muthu, S. Bhowmick, U. V. Waghmare, and A. K. Sood, Symmetry-dependent phonon renormalization in monolayer MoS_2 transistor, *Phys. Rev. B* **85**, 161403(R) (2012).
- [40] S. Das, R. K. Chowdhury, D. Karmakar, S. Das, and S. K. Ray, Substrate-dependent synergistic many-body effects in atomically thin two-dimensional WS_2 , *Phys. Rev. Mater.* **5**, 124001 (2021).
- [41] J. Huang, T. B. Hoang, and M. H. Mikkelsen, Probing the origin of excitonic states in monolayer WSe_2 , *Sci. Rep.* **6**, 1 (2016).
- [42] N. Peimyoo, W. Yang, J. Shang, X. Shen, Y. Wang, and T. Yu, chemically driven tunable light emission of charged and neutral excitons in monolayer WS_2 , *ACS Nano* **8**, 11320 (2014).
- [43] B. Liu, W. Zhao, Z. Ding, I. Verzhbitskiy, L. Li, J. Lu, J. Chen, G. Eda, and K. P. Loh, Engineering bandgaps of monolayer MoS_2 and WS_2 on fluoropolymer substrates by electrostatically tuned many-body effects, *Science* **28**, 6457 (2016).
- [44] X. Hong, J. Kim, S.-F. Shi, Y. Zhang, C. Jin, Y. Sun, S. Tongay, J. Wu, Y. Zhang, and F. Wang, Ultrafast charge transfer in atomically thin MoS_2/WS_2 heterostructures, *Nat. Nanotechnol.* **9**, 682 (2014).
- [45] H. Wu, H. Si, Z. Zhang, Z. Kang, P. Wu, L. Zhou, S. Zhang, Z. Zhang, Q. Liao, and Y. Zhang, All-inorganic perovskite quantum dot-monolayer MoS_2 mixed-dimensional van Der Waals heterostructure for ultrasensitive photodetector, *Adv. Sci.* **5**, 1801219 (2018).
- [46] Q. Fang, Q. Shang, L. Zhao, R. Wang, Z. Zhang, P. Yang, X. Sui, X. Qiu, X. Liu, Q. Zhang, and Y. Zhang, Ultrafast charge transfer in perovskite nanowire/2D transition metal dichalcogenide heterostructures, *J. Phys. Chem. Lett.* **9**, 1655 (2018).
- [47] J. Qiao, F. Feng, S. Song, T. Wang, M. Shen, G. Zhang, X. Yuan, and M. G. Somekh, Perovskite quantum dot-Ta₂NiSe₅ mixed-dimensional van Der Waals heterostructures for high-performance near-infrared photodetection, *Adv. Funct. Mater.* **32**, 2110706 (2022).
- [48] A. Grillo and A. Di Bartolomeo, A current-voltage model for double Schottky barrier devices, *Adv. Electron. Mater.* **7**, 2000979 (2021).
- [49] A. Di Bartolomeo, A. Grillo, F. Urban, L. Iemmo, F. Giubileo, G. Luongo, G. Amato, L. Croin, L. Sun, S.-J. Liang, and L. K. Ang, Asymmetric Schottky contacts in bilayer MoS_2 field effect transistors, *Adv. Funct. Mater.* **28**, 1800657 (2018).
- [50] M. Hussain, S. Aftab, S. H. A. Jaffery, A. Ali, S. Hussain, D. N. Cong, R. Akhtar, Y. Seo, J. Eom, P. Gautam, *et al.*, Asymmetric electrode incorporated 2D GeSe for self-biased and efficient photodetection, *Sci. Rep.* **10**, 1 (2020).
- [51] A. Di Bartolomeo, L. Genovese, T. Foller, F. Giubileo, G. Luongo, L. Croin, S.-J. Liang, L. K. Ang, and M. Schleberger, Electrical transport and persistent photoconductivity in monolayer MoS_2 phototransistors, *Nanotechnology* **28**, 214002 (2017).
- [52] S. Cao, Y. Xing, J. Han, X. Luo, W. Lv, W. Lv, B. Zhang, and Z. Zeng, Ultrahigh-photoresponsive UV photodetector

- based on a BP/ReS₂ heterostructure p–n diode, *Nanoscale* **10**, 16805 (2018).
- [53] Y. Yu, Y. Zhang, X. Song, H. Zhang, M. Cao, Y. Che, H. Dai, J. Yang, H. Zhang, and J. Yao, PbS-Decorated WS₂ phototransistors with fast response, *ACS Photonics* **4**, 950 (2017).
- [54] C. Hu, D. Dong, X. Yang, K. Qiao, D. Yang, H. Deng, S. Yuan, J. Khan, Y. Lan, H. Song, and J. Tang, Synergistic effect of hybrid PbS quantum dots/2D-WSe₂ toward high performance and broadband phototransistors, *Adv. Funct. Mater.* **27**, 1603605 (2017).
- [55] S. Mukherjee, D. Bhattacharya, S. Patra, S. Paul, R. K. Mitra, P. Mahadevan, A. N. Pal, and S. K. Ray, High-responsivity gate-tunable ultraviolet–visible broadband phototransistor based on graphene–WS₂ mixed-dimensional (2D-0D) heterostructure, *ACS Appl. Mater. Interfaces* **14**, 5775 (2022).
- [56] A.-Y. Lee, H.-S. Ra, D.-H. Kwak, M.-H. Jeong, J.-H. Park, Y.-S. Kang, W.-S. Chae, and J.-S. Lee, Hybrid black phosphorus/zero-dimensional quantum dot phototransistors: Tunable photodoping and enhanced photoresponsivity, *ACS Appl. Mater. Interfaces* **10**, 16033 (2018).
- [57] C. Ma, Y. Shi, W. Hu, M. Chiu, Z. Liu, A. Bera, F. Li, H. Wang, L. Li, and T. Wu, Heterostructured WS₂/CH₃NH₃PbI₃ photoconductors with suppressed dark current and enhanced photodetectivity, *Adv. Mater.* **28**, 3683 (2016).
- [58] X. Song, X. Liu, D. Yu, C. Huo, J. Ji, X. Li, S. Zhang, Y. Zou, G. Zhu, Y. Wang, *et al.*, Boosting two-dimensional MoS₂/CsPbBr₃ photodetectors via enhanced light absorbance and interfacial carrier separation, *ACS Appl. Mater. Interfaces* **10**, 2801 (2018).
- [59] H. Wu, Z. Kang, Z. Zhang, Z. Zhang, H. Si, Q. Liao, S. Zhang, J. Wu, X. Zhang, and Y. Zhang, Interfacial charge behavior modulation in perovskite quantum dot-monolayer MoS₂ 0D-2D mixed-dimensional van Der Waals heterostructures, *Adv. Funct. Mater.* **28**, 1802015 (2018).
- [60] R. Lin, X. Li, W. Zheng, and F. Huang, Balanced photodetection in mixed-dimensional phototransistors consisting of CsPbBr₃ quantum dots and few-layer MoS₂, *ACS Appl. Nano Mater.* **2**, 2599 (2019).
- [61] K. Chen, Y. Wang, J. Liu, J. Kang, Y. Ge, W. Huang, Z. Lin, Z. Guo, Y. Zhang, and H. Zhang, In situ preparation of a CsPbBr₃/black phosphorus heterostructure with an optimized interface and photodetector application, *Nanoscale* **11**, 16852 (2019).
- [62] H. Wu, Z. Kang, Z. Zhang, H. Si, S. Zhang, Z. Zhang, Q. Liao, and Y. Zhang, Ligand engineering for improved all-inorganic perovskite quantum dot-MoS₂ monolayer mixed dimensional van Der Waals phototransistor, *Small Methods* **3**, 1900117 (2019).
- [63] X. Zou, Y. Li, G. Tang, P. You, and F. Yan, Schottky barrier-controlled black phosphorus/perovskite phototransistors with ultrahigh sensitivity and fast response, *Small* **15**, 1901004 (2019).
- [64] S. Lee, J. Y. Kim, S. Choi, Y. Lee, K.-S. Lee, J. Kim, and J. Joo, Photosensitive N-type doping using perovskite CsPbX₃ quantum dots for two-dimensional MSe₂ (M = Mo and W) field-effect transistors, *ACS Appl. Mater. Interfaces* **12**, 25159 (2020).
- [65] S. Aftab, M. W. Iqbal, A. M. Afzal, M. F. Khan, G. Hussain, H. S. Waheed, and M. A. Kamran, Formation of an MoTe₂ based Schottky junction employing ultra-low and high resistive metal contacts, *RSC Adv.* **9**, 10017 (2019).
- [66] M. H. Yang, K. B. K. Teo, W. I. Milne, and D. G. Hasko, Carbon nanotube Schottky diode and directionally dependent field-effect transistor using asymmetrical contacts, *Appl. Phys. Lett.* **87**, 253116 (2005).